Korean Journal of Chemical Engineering
https://doi.org/10.1007/s11814-024-00233-y

ORIGINAL ARTICLE

Carbon Powders Transforming From Waste PP Materials for Optimization of 8 mol% Yttria-Stabilized Zirconia Nano-Powders

Qiaoyang Sun[1] · Tao Liu[1] · Tianpeng Wen[1] · Jingkun Yu[1]

Received: 29 February 2024 / Revised: 2 July 2024 / Accepted: 22 July 2024

Abstract

The wasted disposable polypropylene medical mask is one of the common waste polypropylene materials. The waste mask is characterized by being non-biodegradable and carelessly discarded, which causes serious environmental issues and resource waste. This study aims to investigate the recycling of waste disposable polypropylene medical masks to address the ecological problem and transform them into amorphous carbon powders via the carbonization coupling with the high-energy ball-milling method. The recycled waste mask was applied as a carbon dispersant to prepare high-quality 8YSZ nano-powders and the obtained carbon dispersant owned smaller particle size and higher specific surface area than the commercial activated carbon powders. The as-obtained 8YSZ nano-powders were well-dispersed and nano-sized, which resulted in high relative density and ionic conductivity for the sintered 8YSZ ceramic body. These findings suggest that the proposed strategy in this study can recycle the waste disposable polypropylene medical mask to prepare amorphous carbon powders as a carbon dispersant for obtaining high-quality 8YSZ nano-powders and also provide an idea for the comprehensive utilization of other waste polymer materials.

Keywords Waste polymer materials · Nanomaterials · High-energy ball-milling · Carbonization process · 8YSZ nano-powders

Introduction

Waste disposable polypropylene medical masks (DPMMs) are the most common polypropylene waste, especially, after the breakout of the COVID-19 pandemic [1–3]. A surge in the consumption of DPMMs has become a problem due to the non-biodegradable characteristics of DPMMs [4]. Most of the waste DPMMs are discarded in landfills or incinerated, polluting the environment and wasting resources [5]. Converting waste DPMMs into high-value-added products could be important and profitable for the environment and industry. Because the main component of waste DPMMs is the porous polypropylene fiber (PP, $(C_3H_6)_n$) with 85.7% carbon content, the waste DPMMs are promising candidates as carbon sources for preparing various carbon materials [6]. According to previous studies, different routes have been proposed to transform the waste PP materials into different carbon materials [7, 8]. Among them, the most common method is thermal cracking. However, the product components and the production process are complex [9, 10]. The other common method is the carbonization method which is cost-effective and easy to handle. However, the as-obtained product is micron-sized due to the size and structural limitation of PP fibers [11, 12]. Therefore, the carbonization method is rational for recycling waste DPMMs. However, appropriate improvement to reduce product size is also critical to producing high-value-added carbon materials.

To obtain small particle size, high-energy ball-milling is a common and effective method used in various materials [13]. In this method, mechanical energy is used to obtain powder refinement without chemical reaction, and simultaneously achieve atomic diffusion, solid-phase reaction, or phase transition in the process, which is one of the material preparation methods for the production of submicron powder, alloy, and compound [14–17]. This technology has attracted much attention because of its simplicity, applicability to a variety of materials, and ability to reduce hard agglomeration, and is a promising method for reducing the particle size of carbon products prepared by the carbonization method. In previous studies [18,

✉ Jingkun Yu
yujk@smm.neu.edu.cn

[1] School of Metallurgy, Northeastern University, Shenyang 110819, China

Published online: 05 August 2024

19], this technology has been successfully used to prepare various powders with small sizes and controllable structures. Nam et al. [20] investigated the effect of ball-milling modes and additives on the structural change and morphological modification of graphite and multi-wall carbon nanotubes. López-Sánchez et al. [21] produced defective few-layered graphene from graphite flakes via the high-energy ball-milling method.

8 mol% yttria-stabilized zirconia (8YSZ) as conventional ceramic powders have been widely used in many fields, such as refractories, electronic ceramics, and biological ceramics, because of their excellent thermomechanical, ionic conductivity, dielectric constant, and biocompatibility [22–26]. Particularly, 8YSZ nano-powders can improve many processing technologies and devices, because 8YSZ nano-powders can provide more grain boundary volume to 8YSZ ceramic bodies than that prepared with conventional coarse-grained powders [27, 28]. However, aggregation is one of the main drawbacks for 8YSZ nano-powders to impede their application. In our previous studies [29], activated carbon can act as a dispersant in modified sol–gel processing to reduce 8YSZ nano-powders agglomeration and benefit the development of a tetragonal phase, attributing to the adsorptive capacity of the activated carbon. In addition, the carbon black powder was used to prepare weakly agglomerated 8YSZ nano-powders via the decomposition of metal nitrates [30]. Thus, finding an alternative carbon material with a higher adsorptive capacity as a dispersant is meaningful to preparing 8YSZ nano-powders. The waste DPMMs with a dense porous structure may be a promising candidate to prepare carbon material dispersant for 8YSZ nano-powders.

This study aims to respond to crucial problems in carbonization and modified sol–gel methods. Our investigation fully utilized the waste DPMMs as the carbon source, and well-dispersed porous submicron graphite powders were prepared by coupling the carbonization method with high-energy ball-milling. Then, high-quality 8YSZ nano-powders were prepared by a modified sol–gel method using the obtained graphite powder as a dispersant. The properties and characteristics of graphite powders and 8YSZ nano-powders were investigated in detail by Fourier-transform infrared measurement, X-ray diffraction, scanning electron microscopy, Brunauer–Emmett–Teller method, etc. to analyze the reaction mechanism in both processing. Our research provides a green and economical method to recycle DPMMs and prepare high-quality 8YSZ nano-powders.

Experimental Procedure

Materials

Waste disposable polypropylene medical masks, concentrated sulfuric acid (H_2SO_4, Sinopharm Chemical Reagent Co. Ltd., P.R. China, 98%), ethanol (C_2H_6O, Sinopharm Chemical Reagent Co. Ltd., P.R. China, 95%), zirconium carbonate basic ($Zr_2(CO_3)O_2(OH)_2$, Sinopharm Chemical Reagent Co. Ltd., P.R. China), acetic acid (CH_3COOH, Sinopharm Chemical Reagent Co. Ltd., P.R. China, 99.5%), citric acid ($C_6H_8O_7$, Sinopharm Chemical Reagent Co. Ltd., P.R. China, 99.5%), yttrium nitrate hexahydrate ($Y(NO_3)_3{\cdot}6H_2O$, Sinopharm Chemical Reagent Co. Ltd., P.R. China, 99.999%), and deionized water.

Synthesis of Submicron-Sized Graphite Powders and Different 8YSZ Nano-Powders

Waste DPMMs were collected and cut into small pieces. 2 g waste DPMMs were mixed with 80 ml concentrated sulfuric acid and then put into an autoclave heated at 120 °C for 10 h to obtain the carbon sources. The as-obtained carbon sources were washed with deionized water to pH ≈ 7. After that, the carbon sources were heated at 900 °C for 2 h via the carbon-bed heat treatment method to obtain graphite powders. The as-obtained graphite powders were further processed via a high-energy ball-milling method using a planetary ball mill to obtain submicron-sized graphite powders. The ball-milling jar and ball were agate, the agent was ethanol, and the ball-to-powder weight ratio was 400. The ball-milling speed was 300 r.p.m and carried out for 12 h.

Appropriate proportions of $Zr_2(CO_3)O_2(OH)_2$, CH_3COOH, and $Y(NO_3)_3{\cdot}6H_2O$ were chosen as starting materials and were dissolved in deionized water under stirring at 70 °C to form a clear mother solution. About 3 mol of the different carbon dispersants (non-additive, commercial activated carbon, graphite carbon powders) with a proportion to 1 molar of total metal cation were added to the mother solution. Then citric acid (the molar ratio of citric acid/metallic ions was 2) was added as a chelating agent to form a black sol. The black sol was dried at 110 °C for 24 h to obtain the precursor powders. The precursor powders after grinding were calcinated from 500 to 900 °C to obtain the final 8YSZ nano-powders. The diagram illustration shows the brief experimental processing in Fig. 1.

Characterization

The crystal structure and phase composition of the as-prepared samples were identified by X-ray diffraction (XRD, D8 Advanced, Bruker, Germany) with Cu-Ka radiation (2 = 0.15406 nm). The functional groups of the as-prepared samples were analyzed in the range from 4000 to 400 cm^{-1} by Fourier-transform infrared measurement (FT-IR, Thermo Scientific Nicolet iS20, USA). The structure of the as-prepared samples was determined by Raman spectroscopy measurements (Raman, Horiba LabRAM HR Evolution, Japan) in the range of 50–4000 cm^{-1}. The

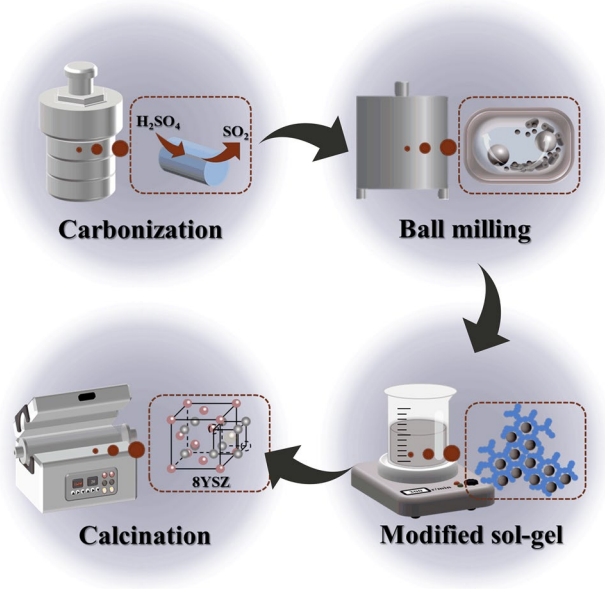

Fig. 1 Diagram illustration of the brief experimental processing

morphology and particle size distribution of the as-prepared samples were characterized by a scanning electron microscope (SEM, Model Ultra Plus, ZEISS). The specific surface area of as-prepared samples was measured by the Brunauer–Emmett–Teller method (BET, Quantachrome Nova 4000e, USA) via nitrogen adsorption tests. The average relative density was calculated by the Archimedes method from ten different ceramic bodies prepared from 8YSZ nano-powders sintered at 1600 °C for 2 h. The electrochemical performance of the as-prepared ceramic body sintered at 1600 °C was measured in the air by the two-probe electrochemical impedance spectroscopy (EIS) method in an electrochemical workstation (AUTO LAB PGSTAT 204 Frequency Response Analyzer).

Results and Discussion

Analysis of the Carbonized Sample

The waste DPMMs after carbonization and heat treatment were examined by XRD, FT-IR, Raman, and SEM. To investigate the phase and crystal structure of the as-obtained sample, the XRD result is shown in (Fig. 2a), there are two broad peaks appeared at 23.3° and 43.8° being characteristic of the amorphous carbon structure [31], indicating that waste DPMMs successfully transformed into amorphous carbon after carbonization and heat treatment. To further investigate the degree of graphitization of the as-obtained sample, the as-obtained sample was examined by the Raman spectrum (as shown in Fig. 2b) where two characteristic peaks located at 1350–1580 cm^{-1} typically correspond to the D and G bonds of the carbon [32]. The nature of the D bond comes from the lattice structure defect of the carbon atom, and the G bond originates from the bond stretching on the surface of the carbon atom [33]. The I_D/I_G ratio (0.86), calculated with the intensity of the D and G peaks, indicates the lower graphitization and high defect of the as-obtained sample, which is attributed to the surface construction of graphite carbon destroyed by the etching of concentrated sulfuric acid during the carbonization process [34]. To examine the functional groups on the surface of the as-obtained sample, the FT-IR spectrum is shown in (Fig. 2c). The major band is located at 1187 cm^{-1} which appeared because of the strong oxidation of concentrated sulfuric acid leading to the destruction of carbon chains and the introduction of sulfonic acid groups [31]. The other band is located at 1605 cm^{-1} attributed to carbon–carbon double bonds which appeared because of the formation of a conjugated system of double-bonded carbon with sulfonic acid sites during the carbonization process [35]. The SEM image was examined and shown in (Fig. 2d) to determine the morphological characteristics of the as-obtained sample. The structure of the as-obtained sample is a porous hollow tube with a diameter of about 10 μm. The reason for the formation of the hollow structure is that the insufficiently carbonized core decomposed during the heat treatment process [36]. Therefore, according to the above results, waste DPMMs can successfully transform into graphite carbon tubes after carbonization and heat treatment.

Analysis of the Graphite Carbon Tubes After High-Energy Ball-Milling

To investigate the effect of high-energy ball-milling on the as-obtained graphite carbon tubes, the samples after ball-milling were examined by XRD, SEM, particle size distribution, and BET method. Compared to the XRD pattern of the carbonized sample, the typical peak (002) of the sample after ball-milling (Fig. 3a) shifts to a lower angle indicating an increasing interlayer space. This may be attributed to the graphite intended to be exfoliated during ball-milling. This is equivalent to an increase in the interplanar distance in the vertical direction which is congruent with plane exfoliation [21]. Meanwhile, the intensity of all peaks for the sample after ball-milling became broader, which is attributed to the decreasing curvature of the carbon tubes during the ball-milling process [20]. Compared to the SEM image of the carbonized sample, as shown in (Fig. 3b), the particle size of the sample after ball-milling is decreased evidently, and the particle is well-dispersed. To further study the particle size of the sample after ball-milling, the particle size histogram was also examined and shown in (Fig. 3c). It can be seen that the particle size distribution of the sample after ball-milling is narrow and the average particle size is only

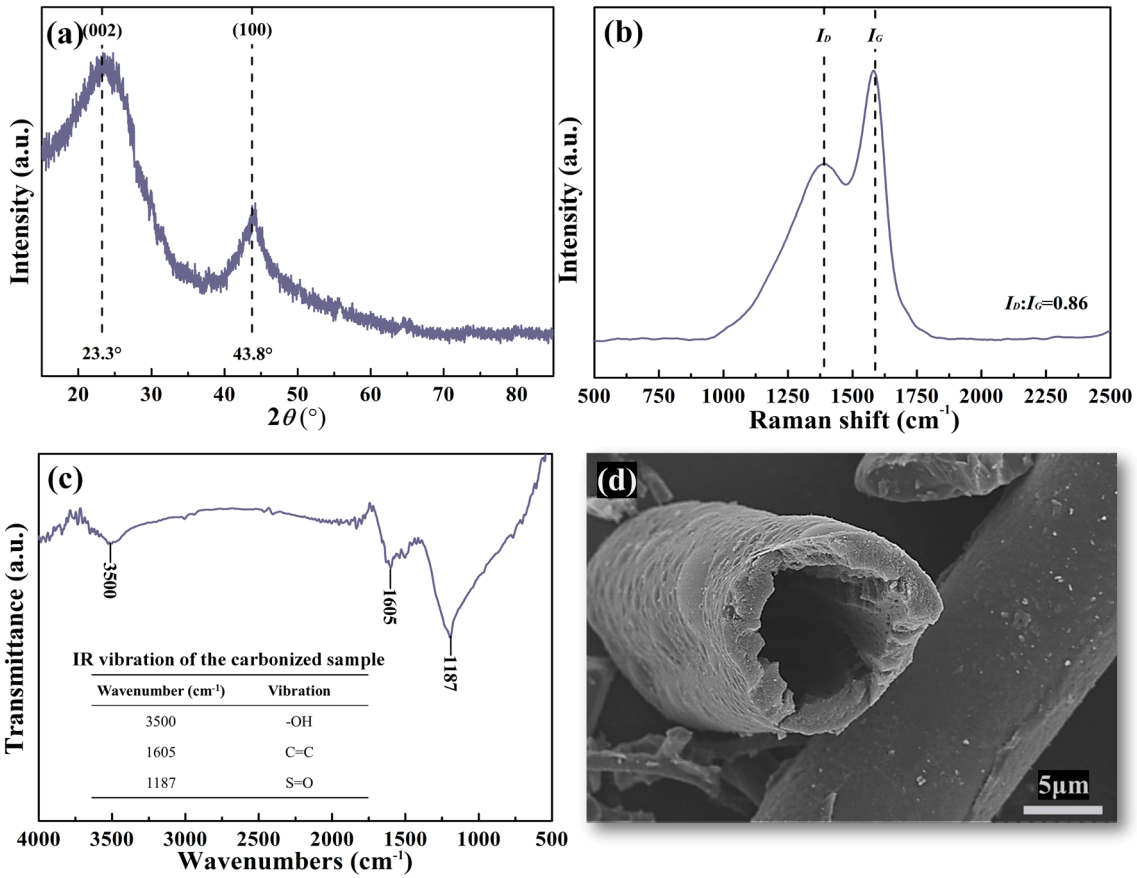

Fig. 2 (**a**) XRD pattern, (**b**) FT-IR spectrum, (**c**) Raman spectrum, and (**d**) SEM image of the graphite powders

0.29 μm. To investigate the adsorptive capacity of the sample after ball-milling, the BET results were examined and shown in (Fig. 3d). The isotherm of the sample after ball-milling exhibits a feature of H2-type isotherm indicating the characteristic of microporous adsorbent [35], and the specific surface area is relatively higher (420.1 $m^2 \cdot g^{-1}$). Therefore, the product of the carbon tubes after the high-energy ball-milling are well-dispersed carbon particles, which own small particle sizes and high specific surface area compared with commercial activated carbon powders (as shown in (Fig. 4a-b).

Combining with all the results, the preparation mechanism of the obtained samples can be considered as follows:

During carbonization, sulfuric acid erodes the PP fibers, resulting in sulfonic acid groups attached to the carbon atoms, forming olefinic unsaturation near 100 °C [37]. However, these sulfonic acid groups are unstable and decompose into isolated C=C double bonds in the range of 100–120 °C, forming two highly reactive allylic sites [38]. These sites facilitate the formation of conjugated sequences of C=C double bonds. Therefore, the surface of pp fiber is carbonized. After heat treatment, the uncarbonized part of the PP fiber core decomposes and the graphite carbon tube is formed finally. In the high-energy ball-milling process, the refinement happened caused by collisions between graphite carbon tubes and balls inside the mill to produce submicron-sized graphite carbon particles (as shown in Fig. 5).

Analysis of 8YSZ Nano-Powders

To investigate the effect of different carbon dispersants on phase and crystallinity evolutions of 8YSZ nano-powders, the XRD patterns of the 8YSZ nano-powders prepared with non-additive (N-8YSZ), commercial activated carbon (CA-8YSZ), and carbonized samples after ball-milling (CS-8YSZ) calcinated from 500 to 900 °C for 2 h are examined and shown in (Fig. 6a). At 500 °C, all powders are crystallographic and pure metastable tetragonal phase ZrO_2 (PDF#48–0224, P42/nmc(137) space group, $c_c = 5.168$). With the increasing calcination temperature, the sharpened peaks gradually appeared and no phase transition can be observed. However, the peaks of AC-8YSZ and CS-8YSZ nano-powders shift to a lower angle, and several peaks split, more evident in the CS-8YSZ sample, indicating the development of the tetragonal phase [39]. To further investigate the phase evolution, the lattice parameters were obtained via

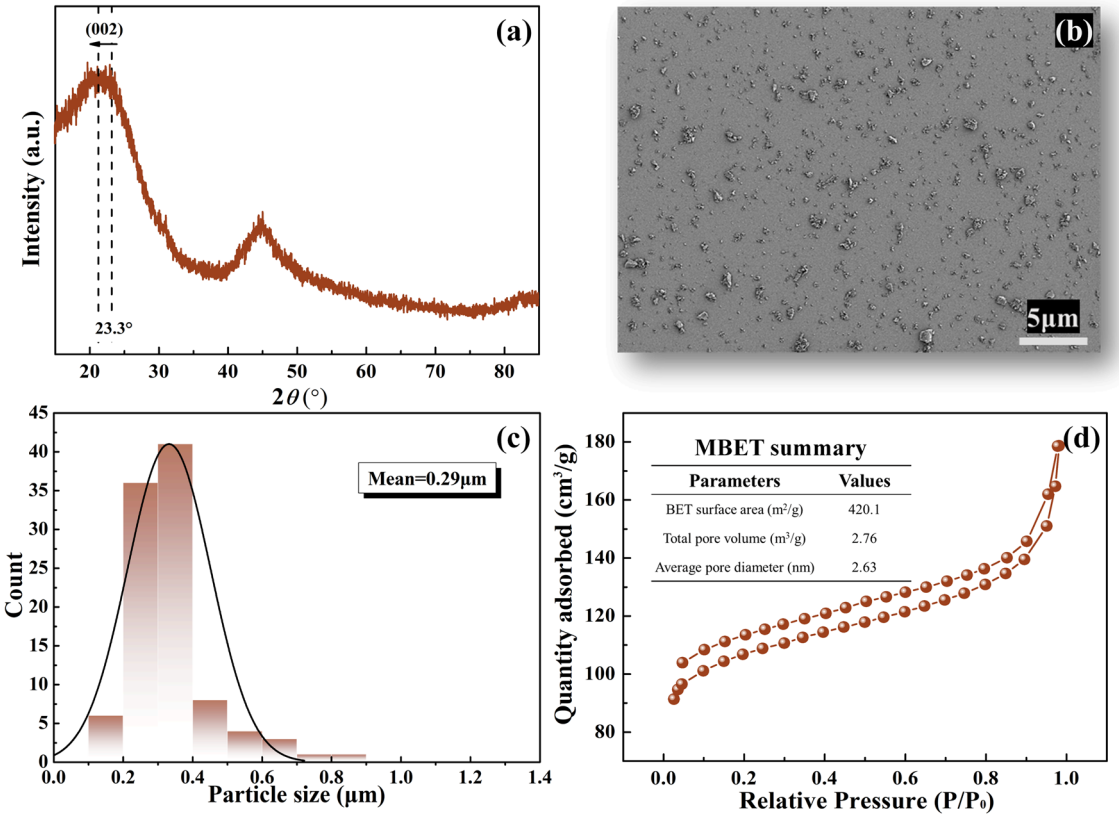

Fig. 3 (**a**) XRD pattern, (**b**) SEM image, (**c**) Particle size distribution, and (**d**) BET results of the graphite powders after high-energy ball-milling for 12 h

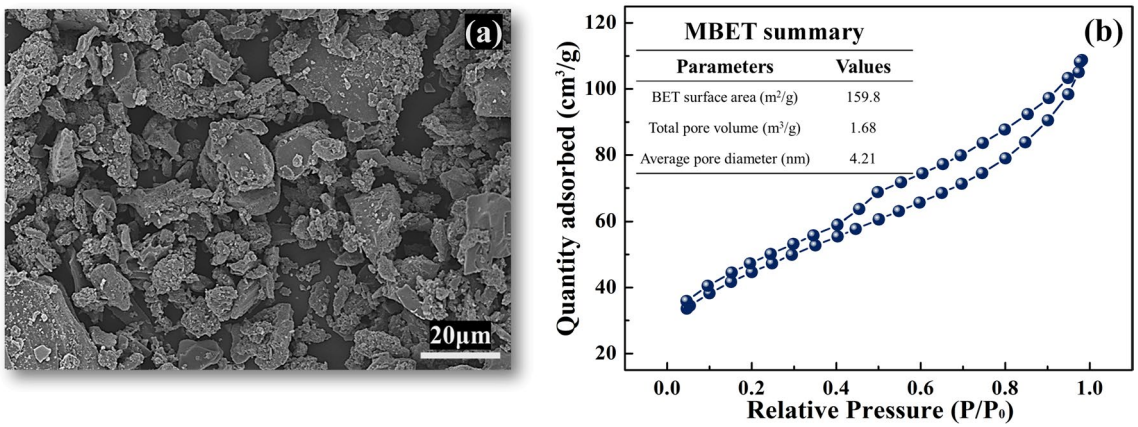

Fig. 4 (**a**) SEM image and (**b**) BET results of the commercial activated carbon powder

the whole pattern refinement module of Jade 6.5 software, and the results are shown in (Fig. 6a). It can be seen that the c_c parameter was increased after adding carbon dispersant, which indicates the stabilization and development of the tetragonal phase. This may be because of the combustion of carbon dispersant using different oxygen, such as lattice oxygen, gaseous oxygen, and gaseous molecules, leading to the introduction of oxygen vacancies in the 8YSZ crystal [40]. These oxygen vacancies decrease the repulsion between oxygen ions leading to the appearance of distortion in the coordination layer, which contributes to releasing the interlayer stress and promoting the stabilization of the tetragonal phase [41, 42]. Compared with AC-8YSZ, CS-8YSZ presents an evident increase in the *c*-direction caused by the sulfonic

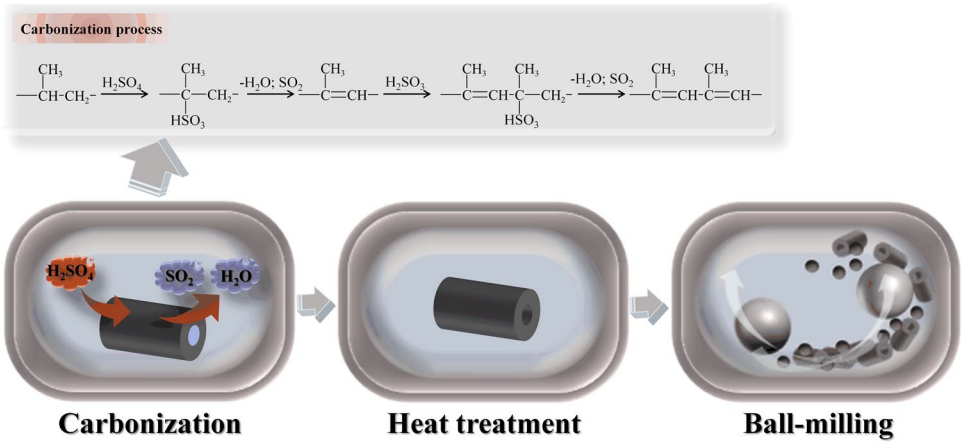

Fig. 5 Diagram illustration of the preparation process

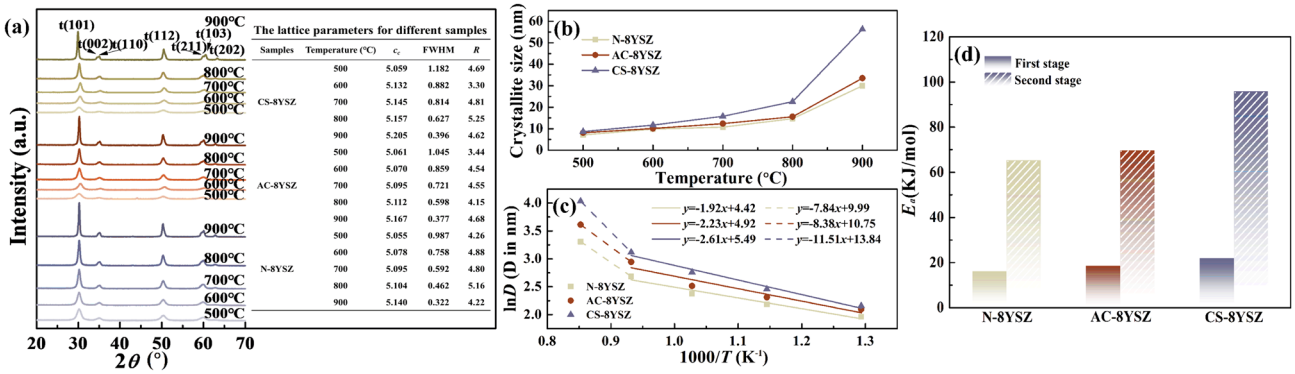

Fig. 6 (**a**) XRD pattern and lattice parameters, (**b**) Average crystallite size, (**c**) ln(D) against 1/T for crystal growth, and (**d**) active energy for crystal growth of 8YSZ nano-powders calcinated from 500 to 900 °C

acid group existing on the surface of the graphite carbon. According to previous studies [43], the phase transformation from the tetragonal to monoclinic phase in 8YSZ starts from the surface region and then gradually proceeds in the bulk. When the sulfonic acid group is adsorbed on the surface, the sulfonic acid group bonds to the surface of the zirconia, which limits the migration of surface atoms and increases the energy required for phase transformation [44]. To investigate the effect of different carbon dispersants on crystal growth behavior, the average crystallite size was calculated by the Scherrer equation [45] and the results are shown in (Fig. 6b). The average crystalline size of as-obtained 8YSZ nano-powders prepared with carbon dispersant was smaller than that with no addition, and 8YSZ nano-powders prepared with carbonized samples after ball-milling own the smallest average crystalline size. This may be because the carbonized sample after ball-milling owns a high adsorptive capacity, which can adsorb and separate the precursors leading to pinning the particle boundaries and stropping particle growth during the nucleation stage [46]. To further study the crystal growth behavior, the activation energy (E) was calculated by the Arrhenius equation [47]. The ln$D$-1/T was plotted in (Fig. 6c) and the activation energy (E) was shown in (Fig. 6d). The CS-8YSZ nano-powders own the highest activation energy because of the addition of carbon dispersant changing the arrangement of the atoms in the precursor structure [48].

To investigate the morphology structure, the SEM images of different 8YSZ nano-powders calcinated at 600 °C were examined and shown in Fig. 7. Among them, CS-8YSZ nano-powders are well-dispersed, attributed to the high adsorptive capacity and gas generation from the decomposition of the carbon dispersant during the calcination process, which can lead to the well-dispersed and loose reactant.

To evaluate the sintering property of different 8YSZ nano-powders, 8YSZ ceramic bodies were synthesized by sintering 8YSZ nano-powders at 1600 °C for 2 h and then measured by Archimedes' method to obtain the relative density as shown in (Fig. 8g). As to the relative density results, the CS-8YSZ ceramic body owns the highest relative density attributed to the well-dispersed and small-sized CS-8YSZ nano-powders. To further investigate different 8YSZ ceramic bodies, the SEM images and grain size distribution of ceramic bodies were examined as shown in (Fig. 8a– f).

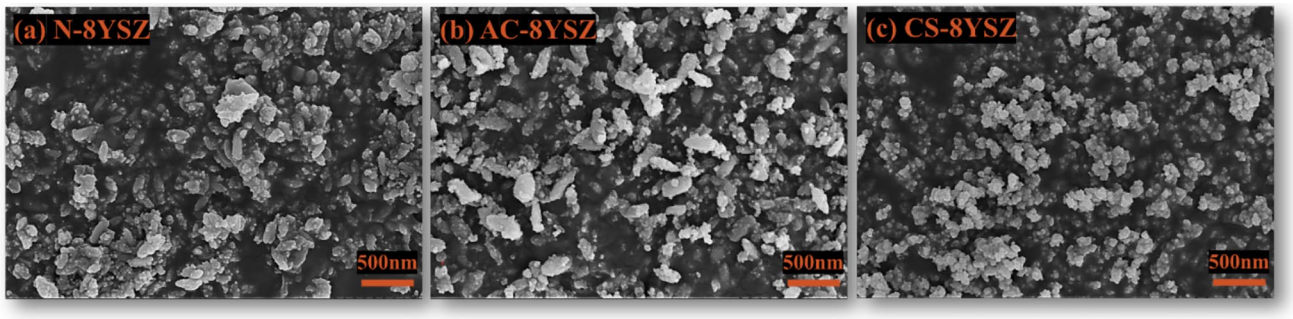

Fig. 7 SEM images of different 8YSZ nano-powders calcinated at 600 ℃

It is noted that the CS-8YSZ ceramic body owns homogeneous grain growth, a narrow grain size distribution, and the smallest average grain size, which may contribute to the high activation energy for CS-8YSZ nano-powders.

To evaluate the electrochemical performance of different sintered ceramic bodies, the electrochemical impedance spectrum (EIS) analysis was conducted from 650 to 900 °C. From Fig. 9, the Nyquist plot is made of one incomplete and complete semi-circle which are related to grain boundary (R_{gb}) and electrodes (R_e) resistance [49]. The total resistance of the ceramic body is the intercept of the grain boundary impedance spectrum with the real axis at high frequencies.

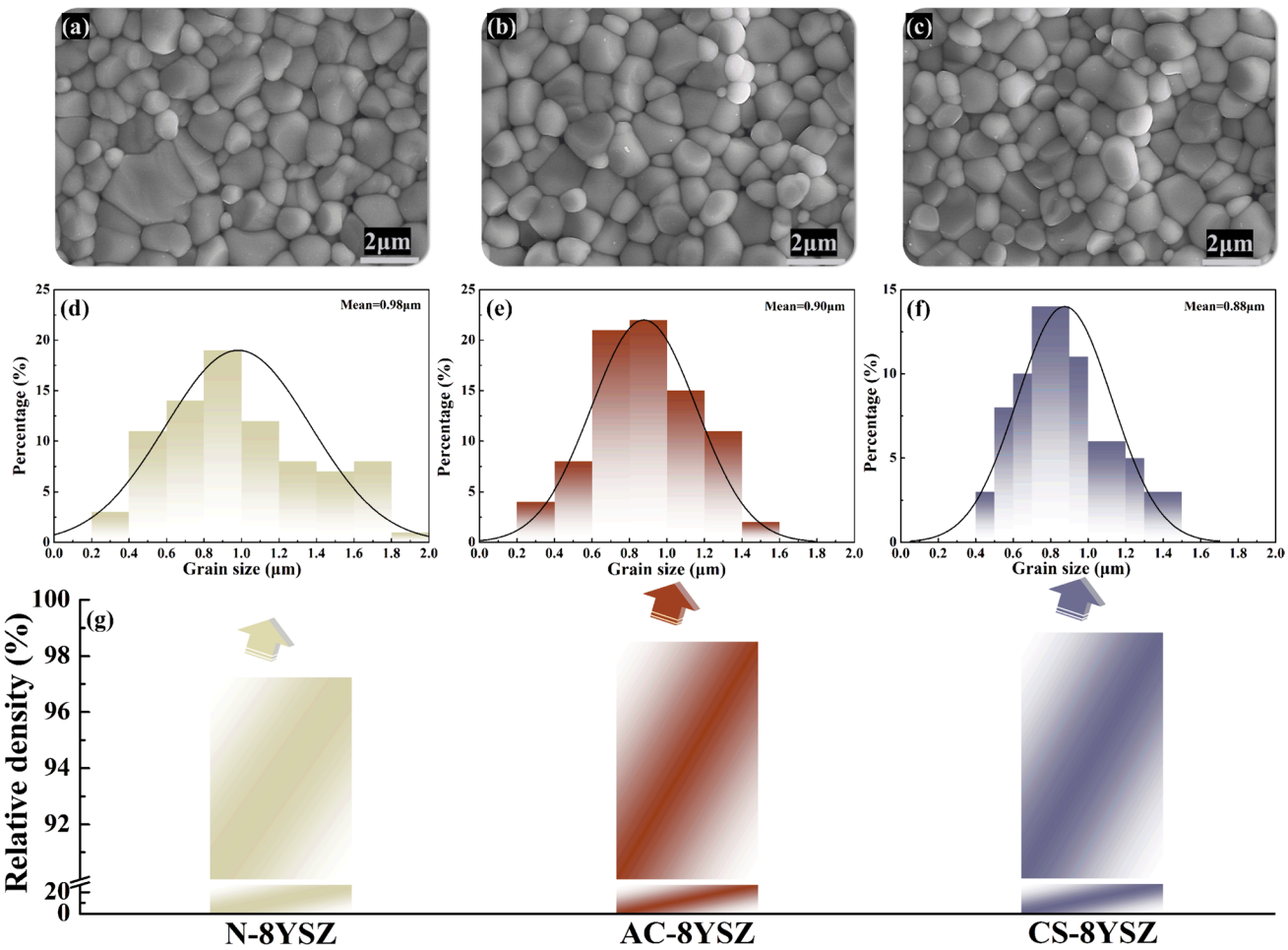

Fig. 8 (**a**-**c**) SEM images, (**d**-**f**) Grain size distribution, (**g**) relative density of different 8YSZ nano-powders sintered at 1600 °C for 2 h

According to Eq. (1), the total ionic conductivity of different sintered samples can be calculated and the results are shown in (Fig. 10a).

$$\sigma = \frac{L}{RS} \tag{1}$$

where σ is the total ionic conductivity, L is the thickness of the 8YSZ ceramic electrode, S is the electrode area of the 8YSZ ceramic electrode, and R is the total resistance of the 8YSZ ceramic electrode. It can be seen from (Fig. 10a), that the ionic conductivity of the CS-8YSZ sintered sample is higher than that of other 8YSZ nano-powders, which may be because of the CS-8YSZ sintered sample with high relative density leading to more efficient oxygen ion diffusion [50]. The Arrhenius' plots and activation energy (E_a) were obtained from Eq. (2) and shown in (Fig. 10b).

$$\sigma = (C/T)\exp\left(-E_a/kT\right) \tag{2}$$

where C is the pre-exponential factor, T is the absolute temperature, and k is Boltzmann's constant (8.6173324×10^{-5} eV·K^{-1}). The results reveal that the activation energy of the CS-8YSZ sintered sample is small. As shown in (Fig. 6a), the lattice parameter of the CS-8YSZ nano-powder increased by adding carbon dispersant, which leads to oxygen ions transferring through oxygen vacancies more easily [51].

Conclusions

A new carbon dispersant was successfully transformed from waste disposable polypropylene medical masks combining the carbonization and high-energy ball-milling method. The resulting carbon dispersant was graphite carbon powders with a submicron-sized and high adsorptive capacity compared with commercial activated carbon powders and have been successfully applied to prepare 8YSZ nano-powders via a modified sol–gel method. The as-obtained 8YSZ nano-powders are well-dispersed and nano-sized, which leads to high relative density and ionic conductivity for the 8YSZ ceramic body. Because of the comprehensive effect of etching of concentrated sulfonic acid in the carbonization method and collision in the high-energy ball-milling method, resulting graphite carbon powders own small particle size and high specific surface area leading to higher adsorptive capacity. The as-obtained graphite carbon powders with high adsorptive capacity can change the arrangement of atoms in the precursor and generate oxygen vacancies as well as gasses in the calcination process to produce

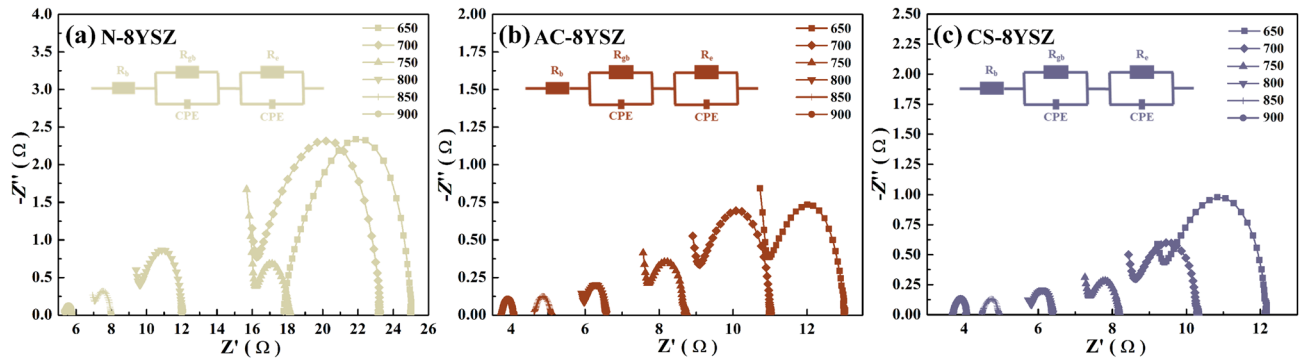

Fig. 9 Impedance spectra of the different sintered samples

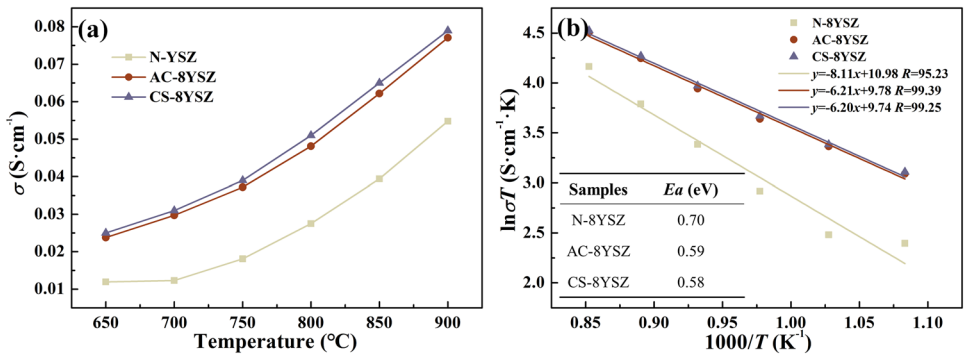

Fig. 10 (**a**) The ionic conductivities and (**b**) Arrhenius' plots and activation energy (Ea) of different sintered samples

8YSZ nano-powders with less agglomeration. This method provides a green and low-cost strategy to recycle waste disposable polypropylene medical masks or even other polymer-based waste materials.

Acknowledgements The authors would like to express their gratitude for the financial support from the National Natural Science Foundation of China (Grant no. 52074070, 51974072, 52204337, and 51874083), the State Key Program of National Natural Science Foundation of China (Grant no. 51932008), China Postdoctoral Science Foundation (2021M700731), and the Fundamental Research Funds for the Central Universities (Grant N2125028).

Author Contributions Qiaoyang Sun: investigation, Writing-original draft, Writing-review & editing, Funding acquisition. Jingkun Yu: conceptualization, Funding acquisition, Supervision. Tianpeng Wen: resources. Tao Liu: supervision.

Data Availability The data that support the findings of this study are available from the corresponding author upon reasonable request.

Declarations

Conflict of Interest The authors declared that they have no conflicts of interest in this work. We declare that we do not have any commercial or associative interest that represents a conflict of interest in connection with the work submitted.

References

1. V. Haldane, C.D. Foo, S.M. Abdalla, A.S. Jung, M. Tan, S.S. Wu, A. Chua, M. Verma, P. Shrestha, S. Singh, T. Perez, S.M. Tan, M. Bartos, S. Mabuchi, M. Bonk, C. McNab, G.K. Werner, R. Panjabi, A. Nordstrom, H. Legido-Quigley, Health systems resilience in managing the COVID-19 pandemic: lessons from 28 countries. Nat. Med. **27**, 964–980 (2021). https://doi.org/10.1038/s41591-021-01381-y
2. L. Liao, W. Xiao, M.V. Zhao, X.Z. Yu, H.T. Wang, Q.Q. Wang, S. Chu, Y. Cui, Can N95 respirators be reused after disinfection? how many times? ACS. Nano. **14**, 6348–6356 (2020). https://doi.org/10.1021/acsnano.0c03597
3. S. Feng, C. Shen, N. Xia, W. Song, M.Z. Fan, B.J. Cowling, Rational use of face masks in the COVID-19 pandemic, lancet. Respir. Med. **8**, 434–436 (2020). https://doi.org/10.1016/s2213-2600(20)30134-x
4. S. Dharmaraj, V. Ashokkumar, S. Hariharan, A. Manibharathi, P.L. Show, C.T. Chong, C. Ngamcharussrivichai, The COVID-19 pandemic face mask waste: a blooming threat to the marine environment. Chemosphere. **287**, 13 (2022). https://doi.org/10.1016/j.chemosphere.2021.132411
5. I. Anastopoulos, I. Pashalidis, Single-use surgical face masks, as a potential source of microplastics: do they act as pollutant carriers? J. Mol. Liq. **326**, 115247 (2021). https://doi.org/10.1016/j.molliq.2020.115247
6. C.W. Zhuo, Y.A. Levendis, Upcycling waste plastics into carbon nanomaterials: a review. J. Appl. Polym. Sci. **131**, 39931 (2014). https://doi.org/10.1002/app.39931
7. T. Tang, X.C. Chen, X.Y. Meng, H. Chen, Y.P. Ding, Synthesis of multiwalled carbon nanotubes by catalytic combustion of polypropylene. Angew. Chem.-Int. Edit. **44**, 1517–1520 (2005). https://doi.org/10.1002/anie.200461506
8. M. Kaneko, H. Sato, Sulfonation of poly(propylene) films with fuming sulfuric acid. Macromol. Chem. Phys. **206**, 456–463 (2005). https://doi.org/10.1002/macp.200400312
9. S. Jung, S. Lee, X. Dou, E.E. Kwon, Valorization of disposable COVID-19 mask through the thermo-chemical process. Chem. Eng. J. **405**, 126658 (2021). https://doi.org/10.1016/j.cej.2020.126658
10. J. Gong, J. Liu, Z.W. Jiang, J.D. Feng, X.C. Chen, L. Wang, E. Mijowska, X. Wen, T. Tang, Striking influence of chain structure of polyethylene on the formation of cup-stacked carbon nanotubes/carbon nanofibers under the combined catalysis of CuBr and NiO. Appl. Catal. B-Environ. **147**, 592–601 (2014). https://doi.org/10.1016/j.apcatb.2013.09.044
11. Y.W. Chao, B.G. Liu, R. Qian, L.B. Zhang, S.H. Guo, Porous carbon materials derived from discarded COVID-19 masks via microwave solvothermal method for lithium-sulfur batteries. Sci. Total. Environ. **817**, 152995 (2022). https://doi.org/10.1016/j.scitotenv.2022.152995
12. S.L. Chen, Z. Liu, S.H. Jiang, H.Q. Hou, Carbonization: a feasible route for reutilization of plastic wastes. Sci. Total. Environ. **710**, 136250 (2020). https://doi.org/10.1016/j.scitotenv.2019.136250
13. A.I. Gusev, A.S. Kurlov, Production of nanocrystalline powders by high-energy ball milling: model and experiment. Nanotechnology. **19**, 265302 (2008). https://doi.org/10.1088/0957-4484/19/26/265302
14. K. Anand, S. Varghese, T. Kurian, Effect of ball size on milling efficiency of zinc oxide dispersions. Part. Sci. Technol. **36**, 308–311 (2018). https://doi.org/10.1080/02726351.2016.1248258
15. Y. Wang, Y. Li, C. Rong, J.P. Liu, Sm–Co hard magnetic nanoparticles prepared by surfactant-assisted ball milling. Nanotechnology. **18**, 465701 (2007). https://doi.org/10.1088/0957-4484/18/46/465701
16. M. Yavuz, H. Maeda, L. Vance, H.K. Liu, S.X. Dou, Effect of ball milling materials and methods on powder processing of Bi2223 superconductors. Supercond. Sci. Technol. **11**, 1153 (1998). https://doi.org/10.1088/0953-2048/11/10/056
17. M.A. Xueming, J.I. Gang, Nanostructured WC/Co alloy prepared by mechanical alloying. J. Alloys Compd. **245**, 30–32 (1996). https://doi.org/10.1016/S0925-8388(96)02678-3
18. S. Coste, G. Bertrand, C. Coddet, E. Gaffet, H. Hahn, H. Sieger, High-energy ball milling of Al_2O_3–TiO_2 powders. J. Alloys Compd. **434–435**, 489–492 (2007). https://doi.org/10.1016/j.jallcom.2006.08.117
19. J. Balogh, L. Bujdosó, G. Faigel, L. Gránásy, T. Kemény, I. Vincze, S. Szabó, H. Bakker, Nucleation controlled transformation in ball milled FeB. Nanostruct. Mater. **2**, 11–18 (1993). https://doi.org/10.1016/0965-9773(93)90045-D
20. H.R. Nam, Y.J. Kim, S.S. Yang, J.-H. Ahn, Ball-milling of graphite and multi-wall carbon nanotubes. J. Nanosci. Nanotechnol. **14**, 9103–9107 (2014). https://doi.org/10.1166/jnn.2014.10096
21. J. López-Sánchez, Á. Peña, A. Serrano, A. Del Campo, ÓR de La Fuente, N. Carmona, D. Matatagui, MDC. Horrillo, J. Rubio-Zuazo, E. Navarro, P. Marín, Generation of defective few-layered graphene mesostructures by high-energy ball milling and their combination with microwires for reinforcing microwave absorbing properties, Appl. Mater. Interfaces. 15 (2023) 3507–3521
22. Z. Xue, Y. Zhu, H. Yu, M. Shi, X. Liu, S. Zhang, Nano-agglomerated powder and thermal shock cycling property of 8YSZ nanostructured thermal barrier coating. Surf. Coat. Technol. **433**, 128173 (2022). https://doi.org/10.1016/j.surfcoat.2022.128173
23. H.T. Li, G.X. Wang, M.Y. Guo, H.Y. Cheng, H. Hu, Z.H. Lin, X.Y. He, Enhancing dispersion of yttria-stabilized tetragonal zirconia nanopowders with microwave solvothermal synthesis. J. Nano Res. **74**, 83–96 (2022). https://doi.org/10.4028/p-rk18uy

24. P.H. Chen, X.Y. Li, F. Tian, Z.Y. Liu, D.J. Hu, T.F. Xie, Q. Liu, J. Li, Fabrication, microstructure, and properties of 8 mol% yttria-stabilized zirconia (8YSZ) transparent ceramics. J. Adv. Ceram. **11**, 1153–1162 (2022). https://doi.org/10.1007/s40145-022-0602-6
25. M. Irshad, K. Siraj, R. Raza, M. Rafique, M. Usman, Q.U. Ain, A. Ghaffar, Evaluation of densification effects on the properties of 8 mol% yttria-stabilized zirconia electrolyte synthesized by cost-effective coprecipitation route. Ceram. Int. **47**, 2857–2863 (2021). https://doi.org/10.1016/j.ceramint.2020.09.140
26. EI. Denisova, AV. Rozhdestvenskaya, VV. Kartashov, Powders based on zirconia for manufacturing solid oxide fuel cell materials, AIP Conference Proceeding (2020), pp. 060003
27. J.X. Zhang, X.W. Huang, H. Zhang, Q.N. Xue, H. Xu, L.S. Wang, Z.Y. Feng, The effect of powder grain size on the microstructure and electrical properties of 8 mol% Y_2O_3-stabilized ZrO_2. RSC Adv. **7**, 39153–39159 (2017). https://doi.org/10.1039/c7ra06710k
28. F. Petrakli, M. Arkas, A. Tsetsekou, α-Alumina nanospheres from nano-dispersed boehmite synthesized by a wet chemical route. J. Am. Ceram. Soc. **101**, 3508–3519 (2018). https://doi.org/10.1111/jace.15487
29. Q.Y. Sun, T. Liu, T.P. Wen, J.K. Yu, Optimization of particle size, dispersity, and conductivity of 8 mol% Y_2O_3 doped tetragonal zirconia polycrystalline nanopowder prepared by modified sol-gel method via activated carbon absorption. J. Eur. Ceram. Soc. **42**, 5831–5841 (2022). https://doi.org/10.1016/j.jeurceramsoc.2022.06.017
30. S.S. Jiang, G.C. Stangle, V.R.W. Amarakoon, W.A. Schulze, Synthesis of yttria-stabilized zirconia nanoparticles by decomposition of metal nitrates coated on carbon powder. J. Mater. Res. **11**, 2318–2324 (1996). https://doi.org/10.1557/JMR.1996.0295
31. X. Hu, Z.D. Lin, Transforming waste polypropylene face masks into S-doped porous carbon as the cathode electrode for supercapacitors. Ionics **27**, 2169–2179 (2021). https://doi.org/10.1007/s11581-021-03949-7
32. Y. Liu, Z. Sun, X. Sun, Y. Lin, K. Tan, J. Sun, L. Liang, L. Hou, C. Yuan, Construction of hierarchical nanotubes assembled from ultrathin V_3S_4@C nanosheets towards alkali-ion batteries with ion-dependent electrochemical mechanisms. Angew. Chem. Int. Ed. **59**, 2473–2482 (2020). https://doi.org/10.1002/anie.201913343
33. J.M. Vallerot, X. Bourrat, A. Mouchon, G. Chollon, Quantitative structural and textural assessment of laminar hydrocarbons through Raman spectroscopy, electron diffraction and few other techniques. Carbon. **44**, 1833–1844 (2006). https://doi.org/10.1016/j.carbon.2005.12.029
34. B. Xie, L. Hong, P. Chen, B. Zhu, Effect of sulfonation with concentrated sulfuric acid on the composition and carbonizability of LLDPE fibers. Polym. Bull. **73**, 891–908 (2016). https://doi.org/10.1007/s00289-015-1525-y
35. K.S.W. Sing, Reporting physisorption data for gas-solid systems with special reference to the determination of surface area and porosity. IUPAC. **54**, 2201–2218 (1982)
36. Q.Y. Sun, T. Liu, T.P. Wen, J.K. Yu, Coupling of carbonization method with high-energy ball milling: towards submicron-sized graphite powders transforming from waste COVID-19 masks. Mater. Chem. Phys. **307**, 128134 (2023)
37. H. Asthana, B.L. Erickson, L.T. Drzal, Sulfonation of polymer surfaces – II. chemical changes on polypropylene and polystyrene surfaces after gas phase sulfonation. J. Adhes. Sci. Technol **11**, 1269–1288 (1997). https://doi.org/10.1163/156856197X00138
38. I. Karacan, H. Benli, Use of sulfonation procedure for the development of thermally stabilized isotactic polypropylene fibers prior to carbonization. J. Appl. Polym. Sci. **123**, 234–245 (2012). https://doi.org/10.1002/app.34454
39. R.E. Juarez, D.G. Lamas, G.E. Lascalea, N.E.W. de Reca, Synthesis of nanocrystalline zirconia powders for TZP ceramics by a nitrate-citrate combustion route. J. Eur. Ceram. Soc. **20**, 133–138 (2000). https://doi.org/10.1016/s0955-2219(99)00146-6
40. M.I. Osendi, J.S. Moya, C.J. Serna, J. Soria, Metastability of tetragonal zirconia powders. J. Am. Ceram. Soc. **68**, 135–139 (1985). https://doi.org/10.1111/j.1151-2916.1985.tb09651.x
41. M.O. Zacate, L. Minervini, D.J. Bradfield, R.W. Grimes, K.E. Sickafus, Defect cluster formation in M_2O_3-doped cubic ZrO_2. Solid. State. Ionics. **128**, 243–254 (2000). https://doi.org/10.1016/S0167-2738(99)00348-3
42. Q. Zeming, S. Chaoshu, W. Yaguang, W. Zheng, L. Tao, H. Tiandou, Z. Zongyan, L. Fuli, An EXAFS study of the nanocrystalline transformation of ZrO_2:Y_2O_3(5%). J. Phys. Condens. Matter. **13**, 11503 (2001). https://doi.org/10.1088/0953-8984/13/50/309
43. M. Li, Z. Feng, G. Xiong, P. Ying, Q. Xin, C. Li, Phase transformation in the surface region of zirconia detected by UV Raman spectroscopy. J. Phys. Chem. B **105**, 8107–8111 (2001). https://doi.org/10.1021/jp010526l
44. C. Li, M. Li, UV Raman spectroscopic study on the phase transformation of ZrO_2, Y_2O_3–ZrO_2 and SO_4^{2-}/ZrO_2. J. Raman Spectrosc. **33**, 301–308 (2002). https://doi.org/10.1002/jrs.863
45. R.E. Juárez, D.G. Lamas, G.E. Lascalea, N.E. Walsöe de Reca, Synthesis of nanocrystalline zirconia powders for TZP ceramics by a nitrate–citrate combustion route. J. Eur. Ceram. Soc. **20**, 133–138 (2000). https://doi.org/10.1016/S0955-2219(99)00146-6
46. M.J. Mayo, Processing of nanocrystalline ceramics from ultrafine particles. Int. Mater. Rev. **41**, 85–115 (1996). https://doi.org/10.1179/imr.1996.41.3.85
47. W.Z. Huang, J.L. Yang, X.S. Meng, Y.L. Cheng, C.J. Wang, B.L. Zou, Z. Khan, Z. Wang, X.G. Cao, Effect of the organic additions on the crystal growth behavior of ZrO_2 nanocrystals prepared via sol-gel process. Chem. Eng. J. **168**, 1360–1368 (2011). https://doi.org/10.1016/j.cej.2011.02.027
48. K. Prabhakaran, A. Melkeri, N.M. Gokhale, S.C. Sharma, Synthesis of nanocrystalline 8 mol% yttria-stabilized zirconia powder from sucrose derived organic precursors. Ceram. Int. **33**, 1551–1555 (2007). https://doi.org/10.1016/j.ceramint.2006.07.002
49. T. Liu, J. Li, M. Yi, Y. Mo, X. Wang, H. Du, X. Yin, Conductivity behavior of Fe, Ti singly and doubly doped CaO-ZrO2. J. Alloys Compd. **798**, 431–437 (2019). https://doi.org/10.1016/j.jallcom.2019.05.228
50. X.J. Chen, K.A. Khor, S.H. Chan, L.G. Yu, Influence of microstructure on the ionic conductivity of yttria-stabilized zirconia electrolyte. Mater. Sci. Eng. A **335**, 246–252 (2002). https://doi.org/10.1016/S0921-5093(01)01935-9
51. S.M. Alizadeh, H. Mohebbi, M. Golmohammad, O. Sharifi, F. Farzaneh, Revisiting Fe-doped 8YSZ as the electrolyte of SOFC – from sintering to electrochemical performance. J. Alloys Compd. **938**, 168553 (2023). https://doi.org/10.1016/j.jallcom.2022.168553